



Research papers

Groundwater discharge and saltwater-freshwater mixing in a mangrove wetland over tidal cycles: A field and modeling study



Kang Peng ^{a,b}, James W. Heiss ^c, Xianjun Xie ^{a,b,*}, Lu Yan ^{a,b}, Yamin Deng ^{a,b}, Yiqun Gan ^{a,b}, Qinghua Li ^d, Yanpeng Zhang ^d

^a State Key Laboratory of Biogeology and Environmental Geology & School of Environmental Studies, China University of Geosciences, Wuhan, China

^b State Environmental Protection Key Laboratory of Source Apportionment and Control of Aquatic Pollution, Ministry of Ecology and Environment, 430074 Wuhan, China

^c Department of Environmental, Earth and Atmospheric Sciences, University of Massachusetts Lowell, MA, USA

^d Wuhan Center of China Geological Survey, Wuhan, China

ARTICLE INFO

This manuscript was handled by Huaming Guo, Editor-in-Chief, with the assistance of M. Rajib Hasson Mozumder, Associate Editor

Keywords:

Mangrove wetland
Saltwater-freshwater mixing
Submarine groundwater discharge
Groundwater flow and salt transport modeling
Multi-level groundwater monitoring profile
Salinity-dependent ecosystem

ABSTRACT

Material transport and transformations in mangrove wetlands are closely related to seawater-groundwater mixing processes, which can influence mangrove growth and development. Therefore, a clearer understanding of groundwater and salt transport dynamics in aquifers beneath mangrove wetlands is needed to accurately estimate chemical fluxes to mangrove ecosystems. We established a multi-level groundwater monitoring profile in a mangrove wetland and constructed a numerical model of tidally-driven groundwater flow and salt transport that was calibrated to salinity and pore water pressure. Model results indicated that 99% of groundwater discharge to the mangrove wetland was saltwater and that this discharge accounted for 33% of total discharge over a spring-neap tidal cycle. Tidal creeks that cross-cut the wetland received the remaining 67% of total discharge. Seawater infiltration from tidal action across the wetland formed a subsurface saltwater-freshwater mixing zone with a geometry that followed the undulation of a high permeable layer at depth. Model sensitivity tests showed that salinity distributions and groundwater discharge patterns were controlled strongly by wetland topography and anisotropy. Model cases with a gently sloping and flat mangrove platform led to substantially less salt mass in the subsurface compared to the base case with mangrove topographic relief. Models with lower anisotropy allowed salt to penetrate through the high-permeability layer to the base of the aquifer. The spatial patterns of fresh and saline groundwater discharge and mixing processes within mangrove wetlands as shown in this study may have implications for mangrove tree nutrient availability and for the prevalence and spatial distribution of mangroves along coastlines.

1. Introduction

Submarine groundwater discharge (SGD) contributes large quantities of dissolved constituents to coastal waters along coastlines worldwide, and is composed of recirculated saline (saline SGD) and fresh groundwater (fresh SGD) (Moore, 2010; Robinson et al., 2018; Santos et al., 2021). Fresh SGD can be highly enriched in dissolved matter relative to surface water (Weinstein et al., 2011) and affects coastal ecosystem stability, functioning, and productivity (Santos et al., 2021). Conversely, in the opposite direction, the landward movement of saltwater (e.g. due to sea level rise) can alter pore water chemistry in

wetland soils, leading to coastal forest loss, expansion of invasive species, and other adverse impacts (Tully et al., 2019). Mangrove wetlands, as the only land-sea boundary forest, are sensitive to both groundwater and salinity (Alongi and Brinkman, 2011). Therefore, it is important to characterize the magnitudes and spatial patterns of fresh and saline SGD for understanding whole-ecosystem scale chemical budgets in mangrove environments. Further, improved insight into aquifer salinity distributions in mangrove wetlands is critical for better understanding controls on the structure and extent of mangrove forests.

Studies of coastal groundwater systems have primarily focused on sandy shorelines (Robinson et al., 2018; Geng et al., 2020), and these

* Corresponding author at: State Key Laboratory of Biogeology and Environmental Geology & School of Environmental Studies, China University of Geosciences, Wuhan, China.

E-mail address: xjxie@cug.edu.cn (X. Xie).

studies have found that freshwater and saltwater flow paths in permeable aquifers are highly complex due to the combined influences of tides, waves, and variations in topography, geology, and the terrestrial hydraulic gradient (Burnett et al., 2006; Santos et al., 2009; Greskowiak, 2014; Heiss, 2014; Robinson et al., 2014; Geng et al., 2020). This complexity can lead to the formation of salt fingers, which cause groundwater to discharge above the low tide line (Greskowiak, 2014; Shen et al., 2016; Shen et al., 2019; Zhang et al., 2021a,b). Studies have also quantified groundwater-surface water exchanges in salt marshes with similar characteristics to mangroves (Moffett et al., 2012; Hou et al., 2022; Xin et al., 2022). However, most salt marsh studies are based on theoretical modeling (Wilson and Morris, 2012; Xin et al., 2012). Although previous salt marsh studies provide important insight into fluid exchange patterns in mangroves, calibrated models are needed to better characterize groundwater discharge patterns and volumes for coastal aquifers composed of fine sediments.

Recent field studies have quantified fluid exchanges across the aquifer-ocean interface in mangrove wetlands. Li et al. (2022) measured vertical hydraulic gradients and used Darcy's law to estimate exchange rates at multiple points across a mangrove platform. Tait et al. (2017) employed a radium mass balance in multiple mangroves along the Australian coastline and estimated groundwater discharge rates ranging from 1.5 to 30.9 cm/d. More recent studies have observed tidally-driven groundwater exchange rates within the same range (Wadnerkar et al., 2021). When accounting for the global area of mangroves, Tait et al. (2017) estimated that groundwater discharge from mangroves is approximately a fifth of global riverine freshwater flows. These studies revealed important insights into volumes and the probable range of total (fresh and saline) fluid exchanges that can occur in mangrove systems. However, owing to measurement approaches, these studies were unable to compartmentalize fresh and saline groundwater discharge components or characterize spatial patterns in fresh and saline discharge.

Studies within the past decade have used numerical models to characterize pore water flow paths and discharge profiles in mangrove aquifers. Xia and Li (2012) combined a numerical model with field measurements to show that groundwater discharged from a mangrove into an adjacent tidal river through a high-permeability zone that outcropped into the surface water. Simulations performed by Xiao et al. (2019a) further demonstrated the importance of geologic layering on pore water flow velocities in mangroves; flow velocities were significantly higher in a horizontally continuous sand layer compared to an overlying mud layer. In a numerical model of a mangrove system in China, Xia and Li (2012) found that the tidally-averaged discharge profile was similar to typical fluid exchange profiles along aquifer-ocean interfaces, with infiltration near the high tide line and discharge at the low tide mark. Although groundwater flow and total SGD patterns in mangroves have been well characterized in these studies, aquifer salinity distributions have not been explored in detail. There are also limited studies exploring subsurface flow and transport in mangroves with calibrated numerical models (e.g. Xiao et al. 2019a), which leaves gaps in process-based understanding of fluid exchanges and material transport in mangrove aquifers.

The shortage of field studies investigating pore water salinity in mangroves is likely due to the difficulty of accessing, instrumenting, and traversing mangrove platforms owing to dense vegetation and extensive root systems. Mangrove roots can alter salinity gradients and brackish flow patterns due to salt rejection and evapotranspiration (McGowan and Martin, 2007). These complexities pose logistical and measurement challenges when investigating salinity distributions in the mangrove subsurface. Nevertheless, a targeted field investigation of pore water salinity distributions in a mangrove aquifer is needed to better understand the connection between land and sea within these hydrologically and biologically active systems.

The objectives of this study were to: (1) Characterize spatial and temporal patterns of pore water salinity and fresh and saline SGD in mangrove aquifers influenced by tides and; (2) obtain a mechanistic

understanding of the role of wetland topography and anisotropy in permeability on SGD and saltwater-freshwater mixing in mangrove aquifers. To achieve these goals, we installed a multi-level groundwater monitoring profile in a mangrove wetland and constructed a variable-density variably-saturated numerical groundwater model. The results are the first to demonstrate spatial and temporal patterns of fresh and saline SGD and pore water salinity distributions and dynamics in mangrove aquifers.

2. Field site and measurements

2.1. Study area

This study was conducted in a mangrove wetland located in Dongzhai Harbor, a semi-enclosed bay with a surface area of ~5400 ha located in the northeastern Hainan Island of China. The bay was formed by subsidence during the 1605 Qiongzhou Earthquake (Fig. 1a) (Yan et al., 2021). The site is the first and largest mangrove forest nature reserve in China, with 1750 ha of mangrove forests distributed in the shoals of the intertidal zone. Dongzhai Harbor has a typical tropical monsoon marine climate, with an average annual rainfall of 1,816 mm and an average annual temperature of 23.1 °C (Chen, 2020). The site has irregular semi-diurnal tides and a tidal range of 1.9 m between mean higher high water (MHHW = 2.1 m) and mean lower low water (MLLW = 0.2 m). Mean sea level is 1.3 m above the local tidal datum at the Porchin tidal station (National Marine Data and Information Service (NMDIS), Hainan), which is used as the reference elevation in this study. Surface water salinity gradually increases from ~20 ppt in tidal channels in the upper harbor to ~35 ppt in Pochin Bay outside of the harbor.

The perimeter of Dongzhai Harbor is underlain by a shallow ~30 m thick unconfined Quaternary aquifer of clayey sand. The Neogene confined aquifer lies below the unconfined aquifer and is composed mainly of sandy conglomerate and clastic rock.

2.2. Sampling profile

The field site is near large mariculture ponds ($19^{\circ} 59' 11.04''$ N, $110^{\circ} 34' 18.36''$ E) and is a typical mangrove wetland dominated by the mangrove species *Rhizophora stylosa*. Two existing domestic wells of 8 m depth border the site; one 600 m to the north (GW1) and one 800 m to the south (GW2) (Fig. 1a). These wells were used to assign the landward model boundary condition (See Section 3.2). There are four tidal creeks (TC) that surround the site, with channel depths of ~3 m (TC1), ~2.5 m (TC2), ~2 m (TC3) and ~0.5 m (TC4) (Fig. 1b).

A 220 m east-west multi-level sampling profile was installed across the mangrove and comprised 11 multi-level sampling sites spaced 20–30 m apart. Each sampling site was a well cluster system with eight wells installed to different depths in a 1.4 m diameter circulator configuration (Fig. 1b), for a total of 88 sampling ports. The center well was the deepest (~20 m, reaching aquifer base) with the surrounding wells screened clockwise at depths of 1 m, 3 m, 6 m, 9 m, 12 m, 15 m and 18 m. Before the sampling profile was established, a 21 m sediment core was taken by a drilling rig 4 m east of sampling well S11. The bottom of the core corresponded to the top of the basement clastic rock, thus it represents the full stratigraphic profile and sediment characteristics of the unconfined aquifer at the sampling site. The purpose of the core was to provide a lithologic reference for drill cuttings retrieved during the installation of the monitoring wells.

The multi-level sampling profile was installed from October 28, 2019 to November 15, 2019. The wells were constructed of PVC pipe (OD: 32 mm, ID: 28 mm) with 70 cm screens wrapped in a double-layer of PET gauze. An auger and water jet was used to drill the boreholes and minimize damage to mangrove trees. The lithology of the mangrove sediments was logged at each site as the drill cuttings emerged at the top of the borehole. Once the target depth was achieved, the well casing was inserted into the borehole and 2–5 L of coarse sand was poured down the

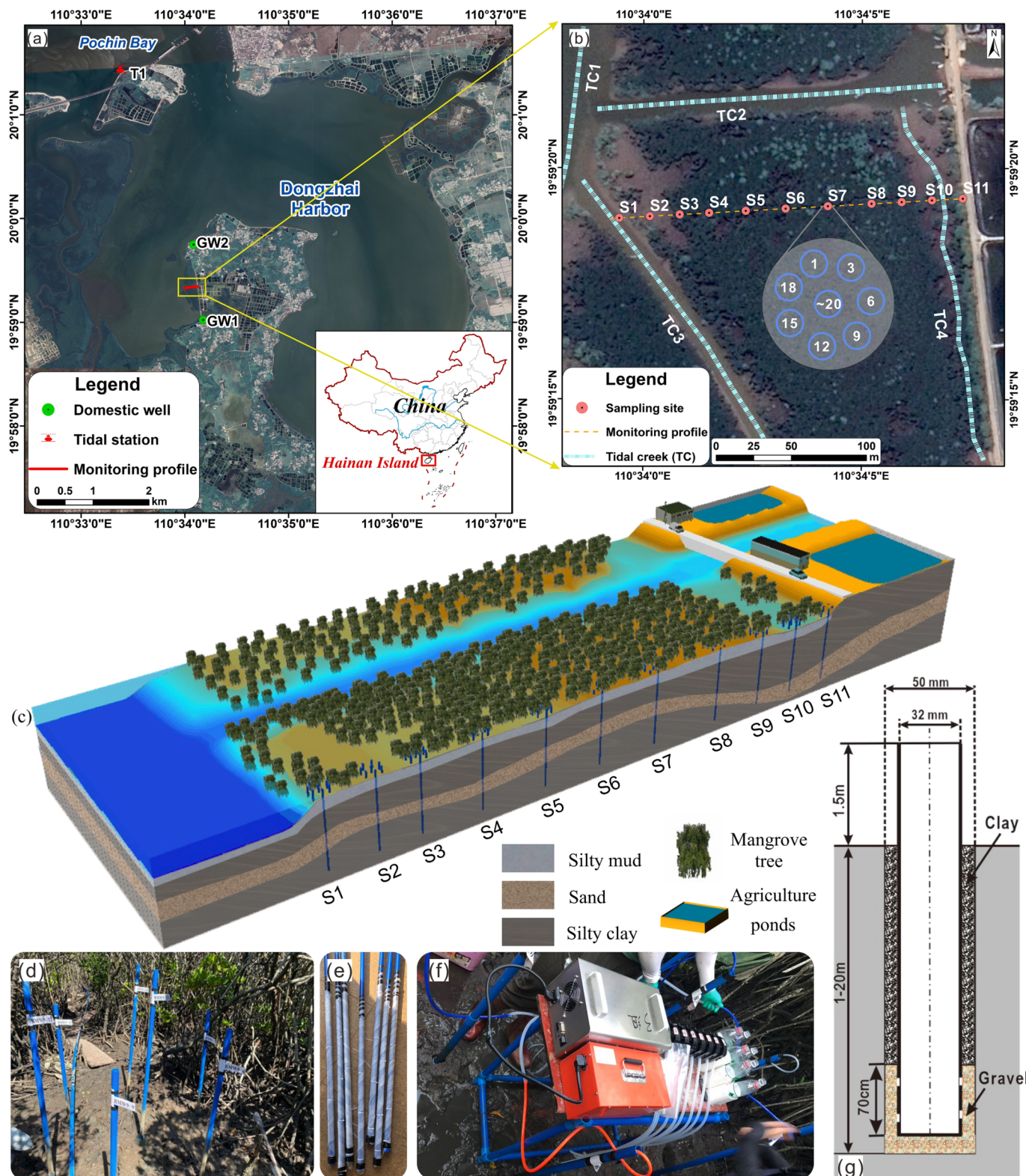


Fig. 1. Study area maps and sampling approach. a) Location of the study site in Dongzhai Harbor and b) sampling profile, tidal creeks, and sampling site locations. The inset shows a schematic of a well cluster used for each of the 11 sampling sites. The numbers in the schematic indicate sampling well depths. c) 3D schematic diagram of the sampling profile and aquifer geology, d) multilevel sampling wells at site S9, e) PVC pipes wrapped with PET screen, f) sampling setup at site S9, and g) schematic of the sampling well construction.

annular space to increase hydraulic connection between the screen and aquifer. The land surface surrounding the well was covered with clay and silt to prevent preferential flow along the casing during high tide. After installation, compressed air was used to clean all well screens and flush out residual fine sediments and groundwater inside the casing. A 10 mm polyurethane pipe was then inserted down the well to the screen for sampling.

2.3. Field measurements

Groundwater samples were collected during three periods: August 21, 2020 - August 29, 2020, January 9, 2021, and July 28, 2021 - July 30, 2021, corresponding to 10, 15, and 21 months after the well transect was installed. The 10 month period between transect installation and the first sampling event ensured that sediment had sufficient time to settle around the well casings to prevent preferential flow from the surface to the screens during inundating tides. A total of 13 groundwater sample sets were collected during daily high or low tide. Preliminary sampling indicated that the subsurface salinity distribution did not change over a tidal cycle, thus the reported cross-sections represent snapshots of salinity over a tidal cycle. Four eight-channel peristaltic pumps were used to sample pore water, for a total of 88 groundwater samples collected at each sampling event ($n = 1,036$ total samples). The pump rate was limited to 100 ml/min to reduce the possibility of drawing in pore water from nearby sample ports. During each sampling event one surface water sample was also collected near S1. Salinity was measured with a calibrated portable multimeter (model HQ40d, Hach Company) and is reported as parts per thousand (ppt). In addition, during the first sampling period, four in-situ loggers (model 3001, Solinst Levelogger LTC) were deployed to measure hydraulic head at 5 min intervals in wells S1-21, S6-3, S9-21 and S11-21 (number after the site number indicates well depth). The loggers were placed at the bottom of well screens to prevent interference during pumping.

The hydrostratigraphy of the aquifer was determined from sediment debris flushed out of boreholes during well installation, as well as

regional geological data. The aquifer is composed a silty mud layer (Layer 1), a silty clay layer (Layer 2), a medium-fine sand layer (Layer 3) of variable depth, a slit clay layer (Layer 4), and a shell-clastic rock layer (not shown), which is the effective base of the unconfined aquifer (Fig. 2). Falling head tests were used to measure the hydraulic conductivity of each of the four layers. Due to many mangrove roots and animal burrows in the top silty mud layer (Alongi and Sasekumar, 1992), the hydraulic conductivity (K) of Layer 1 was relatively high at $1.0 \sim 2.8$ m/d. The measured K value of the silty clay sediment in Layer 2 and 4 was $0.1 \sim 0.5$ m/d and $3.6 \sim 7.2$ m/d for the medium to fine sand layer (Layer 3). The anisotropy coefficient of each layer was determined during model calibration (Table 2). The topography along the sampling profile was measured by combining differential leveling and 3D-LiDAR. The 3D-LiDAR data was used to translate the relative heights from the level measurements to the local tidal datum. The elevation survey indicated that the highest elevation between S1 - S11 was 1.8 m near S8 and the lowest elevation was 0.8 m near TC4 at S11. The overall slope of the mangrove platform was approximately 0.01.

3. Numerical model

A variably-saturated, variable-density groundwater flow and solute transport model was constructed of the groundwater system at the field site to support the interpretation of observations and provide insight into mangrove wetland groundwater discharge patterns. The subsurface flow code PFLOTRAN (Hammond et al., 2014) was employed to simulate porous flow and salt transport in the same 2D cross-shore aquifer section as the sampling profile. PFLOTRAN solves the partial differential equations governing flow and solute transport in saturated and unsaturated porous media using a finite-volume approach and a fully implicit Newton-Raphson algorithm. Within PFLOTRAN, the van Genuchten model is used to represent the relationship between capillary pressure and saturation. The storage and release of water due to sediment compressibility (Reeves et al., 2000; Wilson and Gardner, 2006) was not considered because Xin et al. (2009) found that fluxes due to sediment

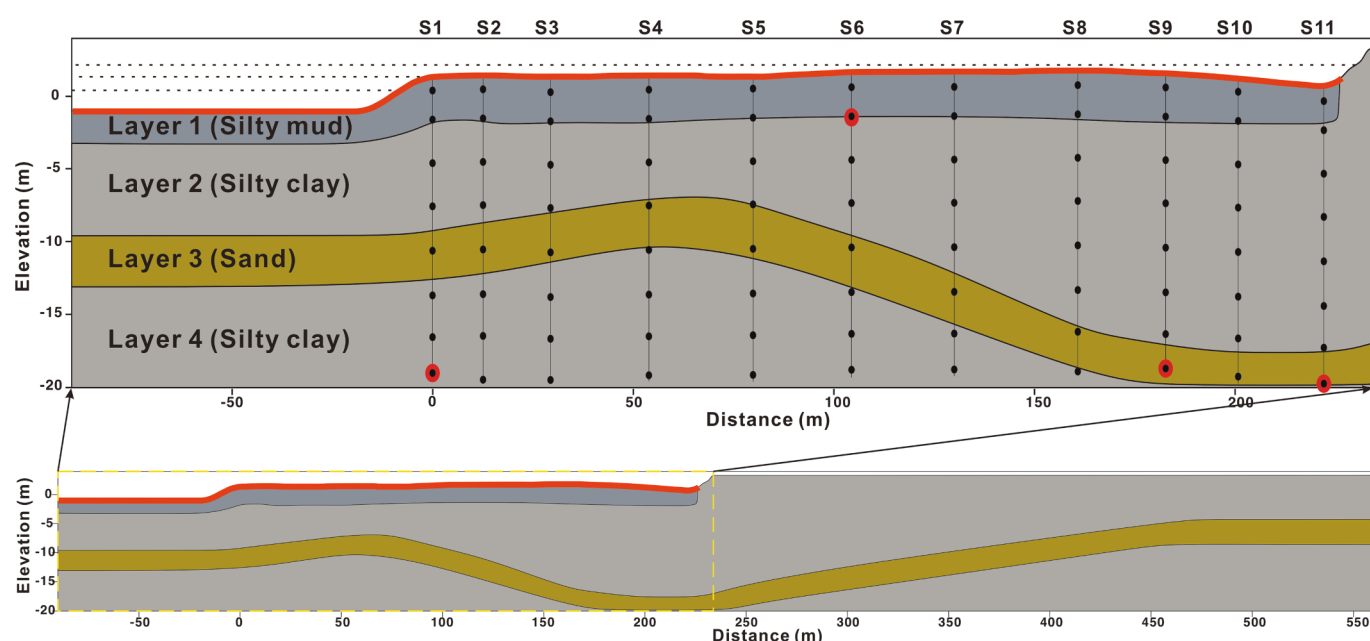


Fig. 2. Conceptual diagram of the model domain, boundary conditions, stratigraphy, and sampling site locations. The red line along the topographic surface shows the combined specified pressure and seepage boundary used to represent tidal forcing. The green vertical line on the far right side of the bottom panel shows the hydrostatic pressure boundary for representing freshwater inflow. In the top panel, the three horizontal black lines in the surface water show, from top to bottom, the high tide level, mean sea level, and low tide level, respectively. The solid black circles are the locations of each sampling well screen. The well screens with red outer circles indicate the location of pressure loggers. Elevation is relative to the local tidal datum. (For interpretation of the references to colour in this figure legend, the reader is referred to the web version of this article.)

compressibility in tidally-influenced systems are negligible when the K value is above 10^{-6} m/s, and the K values in the present study were above that threshold. With the modeling framework described below, the simulations were able to capture tidally-driven flow and saltwater-freshwater mixing processes within the multi-layered mangrove aquifer.

3.1. Model framework

The model domain extended 80 m seaward of S1 and 330 m landward of S11 (Fig. 2). The inland extent of the model was set to where the ratio of the amplitude of hydraulic head fluctuations in the aquifer to the tidal amplitude decreased to 1% (Ferris, 1952; Todd and Mays, 2004). The hydrostratigraphy of the aquifer underlying the mangrove was based on the borehole and falling head test data collected across the sampling profile (Fig. 2). Borehole records show that the top elevation of the clastic rock at the bottom of the aquifer varies by less than 2 m in the vertical direction along the length of the sampling transect, therefore the bottom of the model was set as a horizontal impermeable boundary.

The model grid was refined near the land surface in the intertidal zone where groundwater flow velocities and concentration gradients were higher. Within this zone the horizontal and vertical grid sizes were 0.5 m and 0.0625 m, respectively. Grid cell size in the deeper areas of the aquifer and areas landward of the intertidal zone reached a maximum of 0.5 and 10 m in the vertical and horizontal directions, respectively. Established guidelines recommend the Péclet number ($Pe = \frac{v\Delta t}{\alpha_L} \leq 4$) and Courant number ($Cr = \frac{v\Delta t}{\Delta L} \leq 1$) be below threshold values to minimize numerical oscillations (Chang and Wang, 2002; Voss and Provost, 2002). In these criteria, ΔL is the distance between two adjacent element faces, α_L is the longitudinal dispersivity, and v is the fluid velocity. In the subtidal and intertidal zone, the maximum Cr is about 0.13, satisfying the criteria. Seaward of $x = 250$ m, the maximum Pe in the x and z directions are 3.3 and 0.5, respectively, satisfying the Pe condition. Landward of $x = 250$ m, the maximum Pe in the x and z directions are 10 and 0.5, respectively. Although the Pe in the x direction exceeds the critical value in the far landward section of the model domain, we tested the grid size within the $x > 250$ m range of the model, and found that reducing the grid length in the x direction to 0.5 m significantly increased model run time, while having no discernible impact on the flow field and salt distribution.

3.2. Boundary conditions

Boundary conditions were assigned to capture the dominate hydrologic forcings at the study site. The landward vertical boundary was set as a hydrostatic pressure boundary equivalent to a hydraulic head of 2.6 m above the tidal datum. The assigned head was based on the average terrestrial hydraulic gradient (0.2%) measured at GW1 and GW2 during the first sampling period (see Fig. 1a for well locations). A tidally-resolved time-varying specified pressure boundary (Dirichlet type) was assigned to the intertidal zone to mimic tidal forcing, and a seepage face was allowed to form on the mangrove surface. The seepage face boundary was implemented by setting saturated surface grid cells above the tide level to atmospheric pressure, and unsaturated boundary nodes above the tide level to no-flow. The left vertical and bottom boundary as well as the non-inundating land surface were treated as no-flow boundaries.

The time-varying specified pressure at the aquifer-ocean interface was assigned according to the tidally-varying water depth at each inundated model cell. Because the model required long real-world runtimes to reach dynamic steady-state, six tidal constituents with the largest amplitudes at the site were used to develop a continuous synthetic tidal signal to drive the model. The synthetic tidal signal during the one year sampling period adequately matched the measured tides (Fig. S1). The tidal constituents used to generate the tidal signal were obtained by fitting harmonic constituents to measured tidal stage data

from the Porchin tidal station. The included constituents are the principal lunar diurnal (O1), lunar-solar diurnal (K1), principal lunar semidiurnal (M2), principal solar semidiurnal (S2), lunar elliptic semidiurnal (N2) and principal solar diurnal (P1, Table 1). The following formula was used with the 6 constituents:

$$H_t = H_{\text{datum}} + \sum_{i=1}^6 A_i \cos(\omega_i t - \theta_i)$$

where H_t (m) is the tide level varying with time t (d) and H_{MSL} (m) is the tidal datum. For each tidal constituent i , A (m) is the amplitude, ω (rad/d) is the tidal angular frequency, and θ (rad) is the phase.

The transport boundary condition along the aquifer-ocean interface was zero-concentration gradient for outward flow and a constant concentration of 30 ppt for inward flow. The specified concentration of 30 ppt was the average seawater salinity measured in the surface water near S1 during the full monitoring period. A constant concentration of 1 ppt was set along the landward vertical boundary. All no-flow boundaries were set to zero solute flux.

3.3. Model parameters and model cases

This study considers one base model and 4 case models. The base model is calibrated to measurements (Fig. 2) and its parameters are shown in Table 2. All parameters in Table 2 were constant across model cases except for the horizontal and vertical permeability of Layers 1 and 2, which were modified in select model cases. Since only the top silty mud layer (Layer 1) became unsaturated at low tide, the water retention parameters of the deeper layers did not affect model results. The measured vertical anisotropy of Layers 2 and 4 is small (0.05) likely due to the 1605 earthquake that formed the harbor. Following the shaking, pore space between the silt and clay particles in Layers 2 and 4 likely decreased due to grain settlement (Manga and Wang, 2015), resulting in tightly packed sediment and high anisotropy.

The case models were designed to analyze the influence of two key factors on groundwater discharge and pore water salinity in mangrove wetlands: topography (Case-T) and anisotropy (Case-P). Two model cases were run for each factor tested (Fig. S1). Sensitivity to mangrove wetland topography was evaluated by simplifying the intertidal topography to a constant slope in the first Case-T (Case-T1) model, and setting the intertidal topography to a flat profile in Case-T2. In the two Case-P models, anisotropy was varied to test sensitivity to animal burrows and sediment compaction following the 1605 earthquake. In Case-P1, the anisotropy of Layer 1 was increased to characterize the influence of animal burrows on increasing the permeability of the top aquifer layer. The vertical permeability of Layer 1 in the base model was high to account for animal burrows, thus in Case-P1 the vertical permeability of Layer 1 was reduced relative to the base model from 3.15×10^{-12} to 3.15×10^{-13} m² (Layer 1 K_z/K_x changed from 1.0 to 0.1). Model Case-P2 was designed to evaluate the influence of Layer 2 anisotropy that was likely elevated due sediment compaction from the 1605 earthquake. To reflect conditions not influenced by enhanced compaction, the vertical permeability of Layer 2 was increased slightly relative to the base model from 1.05×10^{-14} to 2.10×10^{-14} m² (Layer 2 K_z/K_x changed from 0.05 to 0.1). We note that the chosen anisotropy values are a first-order estimate of the impacts of animal burrows and earthquake compaction, as

Table 1
Tidal constituents used to generate the predicted tidal signal.

Symbol	Amplitude (m)	Phase (rad)	Frequency (rad/day)	Description
O1	0.322	2.854	5.84	Principal lunar diurnal
K1	0.263	1.596	6.30	Lunar-solar diurnal
M2	0.309	1.171	12.14	Principal lunar semidiurnal
S2	0.132	0.716	12.57	Principal solar semidiurnal
N2	0.058	-2.681	11.91	Lunar elliptic semidiurnal
P1	0.085	2.563	6.27	Principal solar diurnal

Table 2
Model parameters in the base model.

Model Parameters	Layer 1 Silty mud	Layer 2 & 4 Silty clay	Layer 3 Sand
Porosity ^a , φ	0.35	0.4	0.3
Longitudinal dispersivity ^b , α_L (m)	1	1	1
Transverse dispersivity ^b , α_T (m)	0.1	0.1	0.1
Horizontal permeability ^a , k_H (m^2)	3.15×10^{-12}	2.10×10^{-13}	5.25×10^{-12}
Vertical permeability ^a , k_V (m^2)	3.15×10^{-12}	1.05×10^{-14}	5.25×10^{-13}
Residual water content ^c , θ_r	0.1	0.2	0.07
Van Genuchten α ^c (Pa^{-1})	1.1×10^{-3}	1.0×10^{-3}	1.2×10^{-3}
Van Genuchten m ^c	0.5	0.5	0.5

^a Calibrated from field measurements.

^b Gelhar et al. (1992).

^c Schwartz et al. (2003).

we lack measurements of burrow geometry and density at the field site, as well as permeability measurements before the earthquake.

Initial salinity distributions were adjusted in each model case to decrease the runtime required to reach quasi-steady state (Fig. S3). Model results were independent of initial salinity distributions, which was confirmed by running the simulations long enough until salinities stabilized. In the base case model, the initial salinity distribution was set similar to the measured salinity distribution, as that distribution required the shortest simulation time to reach quasi-steady state. As Fig. S2 shows, quasi-steady conditions were achieved when long-term total salt mass reached an asymptote. All models ran with 48 Intel Xeon Platinum 8260 cores on the Massachusetts Green High Performance Computing Cluster TX-E1 (Reuther et al., 2018). For the base model with 61,480 active cells and a time step length of one hour, the model required a real-world runtime of 96,000 days to achieve quasi-steady state (Fig. S3), which translated to 115 h of computation time on the cluster. Exchange profiles, streamlines, and flow vectors are reported as the average tidally-averaged flows over two adjacent spring tides (August 19, 2020 to September 2, 2020).

4. Results and discussion

4.1. Field observations

4.1.1. Pore pressure

Pore pressure in the aquifer responded to both tides and groundwater pumping during sample collection. Fig. 3 shows pore pressure measured in four wells during a period when the wells were pumped intermittently. The rapid drop in pore pressure in wells S1-21, S9-21, S11-21 reflected times when water was pumped from the wells to collect pore water samples. The rate of recovery to the initial pressure in each well was indicative of the permeability of the material surrounding the wells screens; well S1-21 had the slowest recovery and thus was installed in lower permeability material. The positive pore pressure spikes in S11-21 were caused by insertion and removal of the pumping hose during sample collection.

The relative difference in pore pressure between wells at 21 m depth at either end of the sampling transect indicated that the flow direction near the base of the aquifer was from land to the ocean. In addition, when sea level was below the land surface, the low-permeability of Layer 1 and the relatively flat mangrove surface caused the water table to drop slowly (Levanon et al., 2017; Marois and Stecher, 2020), resulting in nearly constant pore pressure in well S6-3 over tidal cycles.

4.1.2. Salinity distributions

The measured salinities revealed a region of elevated salinity overlaying fresh groundwater. Fig. 4 shows salinity distributions at the 13 sampling times; values between sample screens were estimated by interpolating salinity using the ordinary kriging method (Fig. 4b). The bottom of the saltwater-freshwater mixing zone was consistent with the spatial extent and shape of the high-permeability sand layer extending from onshore to offshore (Figs. 2 and 4). Freshwater from inland preferentially flowed through the high K layer (Layer 3) instead of Layers 1 and 2 with lower permeability. The freshwater, flowing quickly though Layer 3, transported salt that diffused across the Layer 2–3 boundary seaward. In effect, the high K layer acted as a barrier to downward salt transport because salt was entrained into the freshwater in the high K layer and flushed seaward. Brackish pore water extended to a depth of 8–12 m between S1 and S5 and then increased in depth gradually to 20 m between S6 to S9. The depth to the bottom of mixing zone then decreased from S9 to S11 (Fig. 4).

Salinity fluctuations over the ~1 year sampling period were generally minor, with an average coefficient of variation of salinity below 0.2 across all 88 ports (Fig. S4). Salinity at the marine and inland ends of the transect exhibited relatively larger fluctuations. The coefficient of variation in these sections of the aquifer were greater than 0.5 (Fig. S4). At the inland end, the overall salinity below 12 m depth in wells S10 and S11 decreased over time. A possible reason for this change may be due to irregular inland water pumping from nearby aquaculture, which may have lowered the freshwater hydraulic gradient during the first sampling periods, allowing saline water to intrude inland (Shi and Jiao, 2014) before returning to base line conditions. There was no observed seasonal trend in subsurface salinity across the sampling periods.

Measured salinities showed that salt accumulated near the *Rhizophora stylosa* mangrove root system, which typically extended to a depth of 3 m below the ground surface. Several pore water samples from wells S3 – S9 within this shallow zone were 2–10 ppt higher than surface water. These higher salinities were due to transpiration by the mangroves and exclusion of salt during water uptake by the mangrove roots (Yan and Guizhu, 2007).

4.2. Base model

4.2.1. Comparison to field measurements

Simulated salinities at times corresponding to the first 8 sampling events are shown in Fig. 5. Model cross sections corresponding to the other 7 sampling events are not shown because modeled salinity distributions did not change with time. The overall modeled salinity distribution was similar to the measurements shown in Fig. 4. Comparison

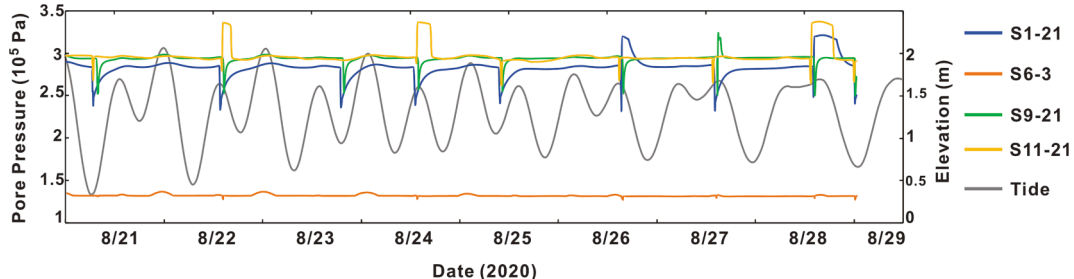


Fig. 3. Time series of pore pressure measured in four wells installed in the mangrove subsurface. The right y-axis shows the tidal stage.

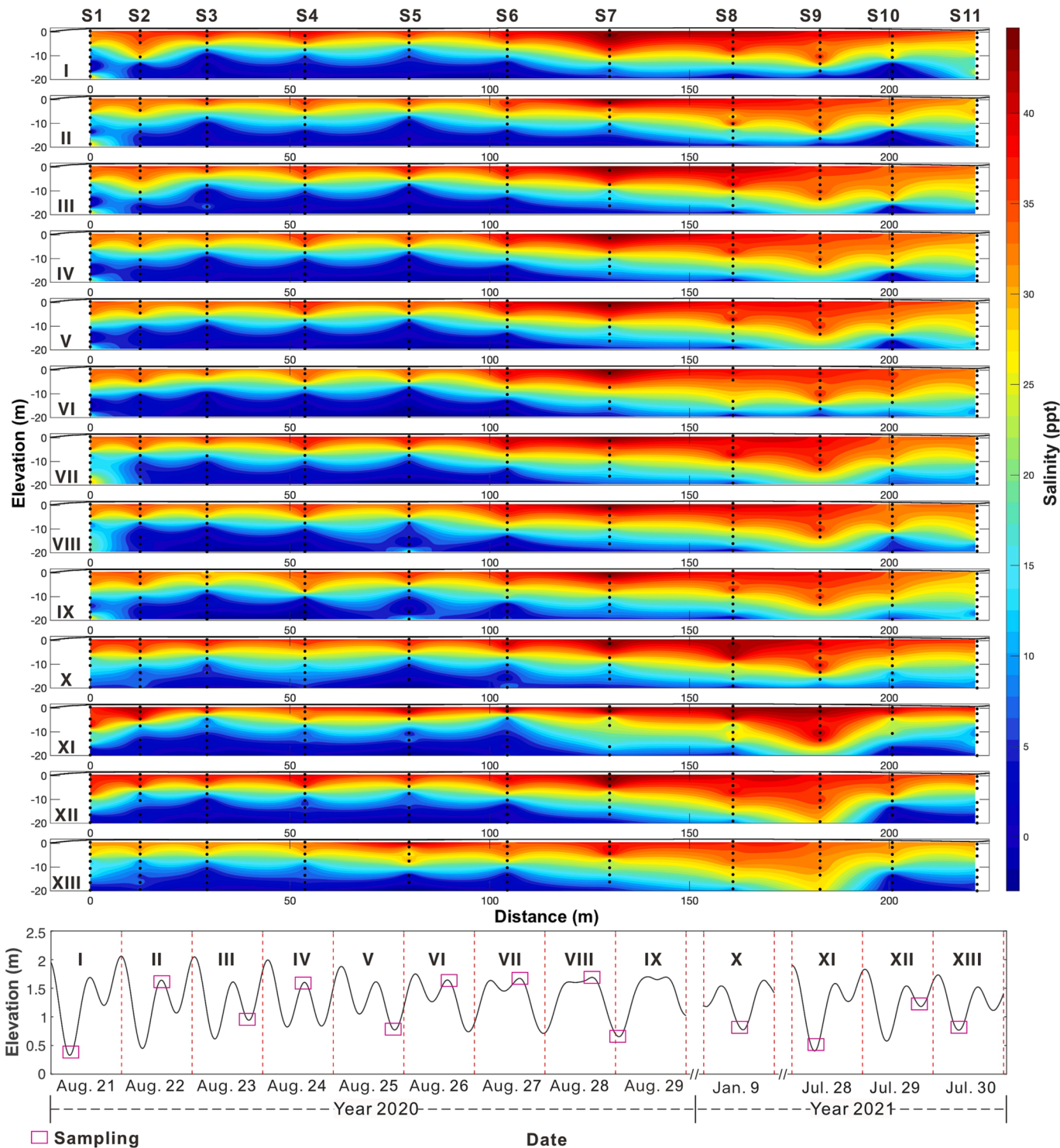


Fig. 4. a) Measured salinity distributions during the 13 sampling events. The black dots indicate the sample port locations. b) Sampling times and tide levels over the 3 sampling periods that spanned the 13 sampling events. Note the breaks in the x-axis showing the three sampling periods. The elevation is relative to the local tidal datum.

between the measured and simulated values at the sample ports showed that 71% of the simulated salinities were within the 5 ppt confidence interval (R-squared of 0.83, mean error of 3.3 ppt) and that the overall fitting results were good (Fig. 6). Large deviations from the measured values were mainly concentrated between sampling sites S9 and S11 where the model underestimated salinities. There was excellent agreement from S1 - S8 in which the mean error was 1 ppt for all depths. Additionally, both our measurements and the simulated salinities

indicated that a lower saltwater freshwater interface was absent below the mangrove wetland (Figs. 4 and 5). The lack of a lower interface was due to the high-permeability layer, which formed a hydraulic barrier to downward flow of saltwater under the bay immediately adjacent to the mangrove platform. Fig. S5 illustrates that a traditional saltwater-freshwater interface forms without the high-permeability layer, highlighting the importance of the layered geology at this site.

Measured and modeled pore water pressures were compared to

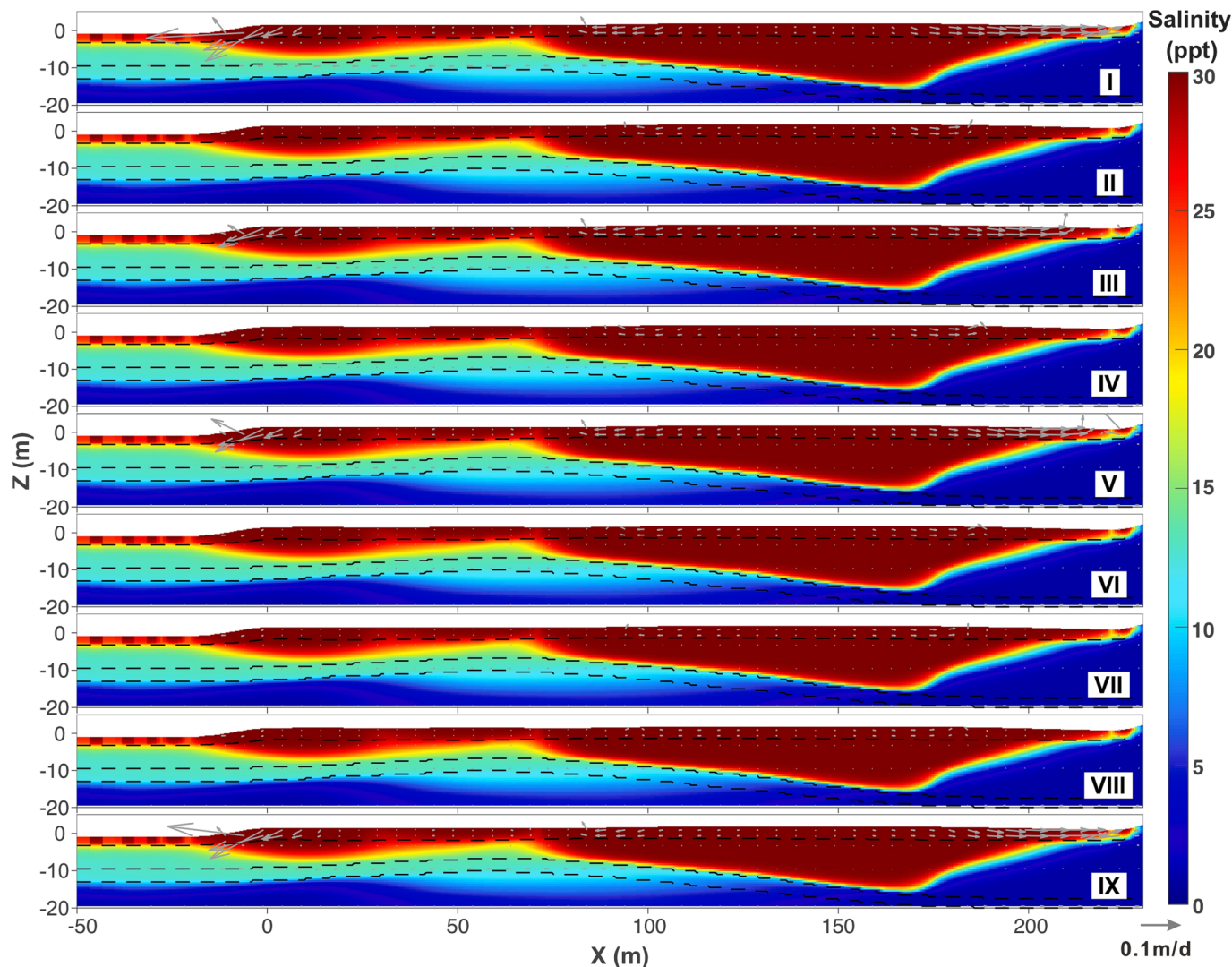


Fig. 5. Simulated salinities at times corresponding to sampling events in the first sampling period. The times correspond to the first 9 panels in Fig. 4. The elevation is relative to the local tidal datum.

provide further insight into the reliability of the model to simulate the groundwater flow system at the Dongzhai Harbor mangrove site. Both the measured and simulated pore pressure exhibited small oscillations in response to the overlying tidal forcing (Fig. 7a-d). The amplitude of the measured oscillations were slightly larger than those modeled, likely because the predicted tidal signal applied in the model was damped relative to the actual tidal water levels (Fig. 7e). Interestingly, the peaks in measured and modeled pressure for wells S1-21 and S11-21 were in phase, with both occurring approximately one hour after high tide despite being on opposite ends of the transect (Fig. 7a and e). The similar lag time was likely due to the tidal creek (TC4) that flowed adjacent to S11 (Fig. 1). The sediments beneath the platform can be regarded as a U-shaped aquifer (Zhang et al., 2020) because TC3, TC2, and TC4 bound the mangrove platform on three sides. With this configuration of tidal creeks the distance from TC4 to S11 was approximately the same as the distance from TC3 to S1. As a result, periodic pressure fluctuations from tides propagated the same distance to S1 and S11, producing similar lag times. There was some discrepancy in observed and modeled pore pressure phases in wells S6-3 and S9-21 (Fig. 7b and c). Measured pore pressures in both wells responded instantaneously to rising tide levels while simulated pressures lagged the tide by approximately one hour. The explanation for the measured instantaneous responses at these two wells is unclear, but may be related to small-scale tidal channels that

were not incorporated into the model and that led to high hydraulic connection of these wells to surface water.

4.2.2. Total SGD and spatial fluid exchange patterns

Given that the model satisfactorily reproduced the measured salinity distribution, salinity dynamics, and pore water pressures, we used the model to quantify total SGD and evaluate spatial variability in SGD. Net outflow, averaged across two spring tidal cycles (new moon to full moon), was $0.40 \text{ m}^3/\text{d}$ (per meter length of shoreline). Net outflow was higher at the two spring tides ($0.48 \text{ m}^3/\text{d}$ and $0.47 \text{ m}^3/\text{d}$) relative to neap tides ($0.35 \text{ m}^3/\text{d}$ and $0.28 \text{ m}^3/\text{d}$) owing to a stronger land-sea hydraulic gradient from the lower tide levels at spring tide. The modeled outflow of $0.40 \text{ m}^3/\text{d}$ was about one tenth of the net outflow of $3.94 \text{ m}^3/\text{d}$ simulated in Xia and Li (2012) for a different mangrove forest in Dongzhai Harbor. This difference is likely due to the more permeable sediments in the mangrove in Xia and Li (2012). In that study a high-permeability zone was only 1.5 m below the surficial low-permeability layer compared to 10 m in this study. The high permeability layer in Xia and Li (2012) also acted to channel water from land to the bay because it outcropped across the bottom of the seafloor. At our site, the high-permeability layer continued offshore, thus all SGD exited the aquifer through silty clay.

SGD was compartmentalized into three main zones based on the

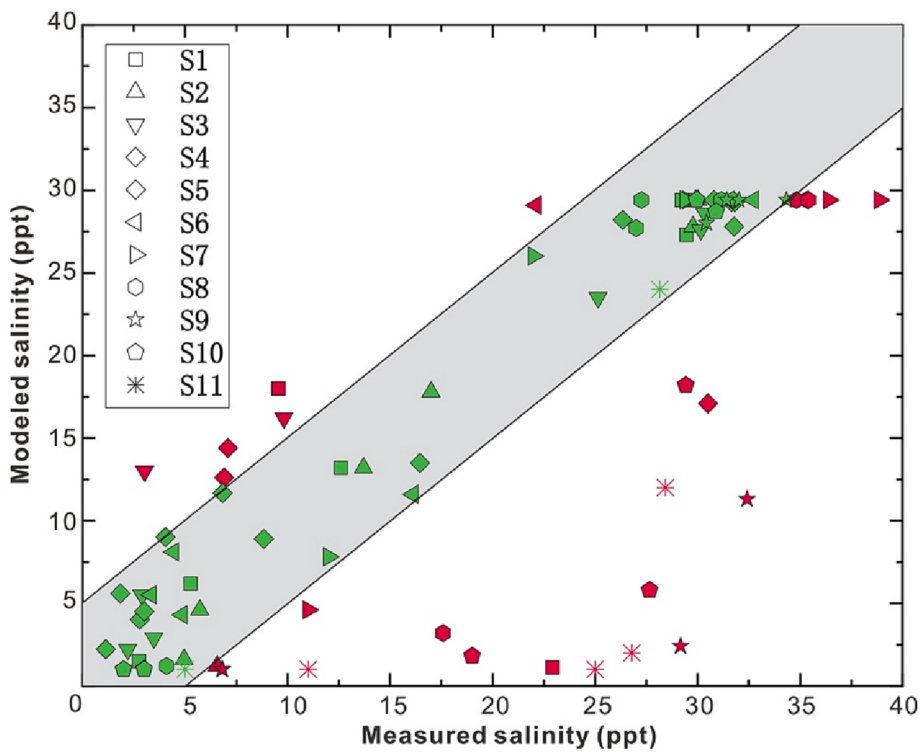


Fig. 6. Comparison between measured and modeled salinity at each sampling port. The gray area indicates the confidence interval of 5 ppt.

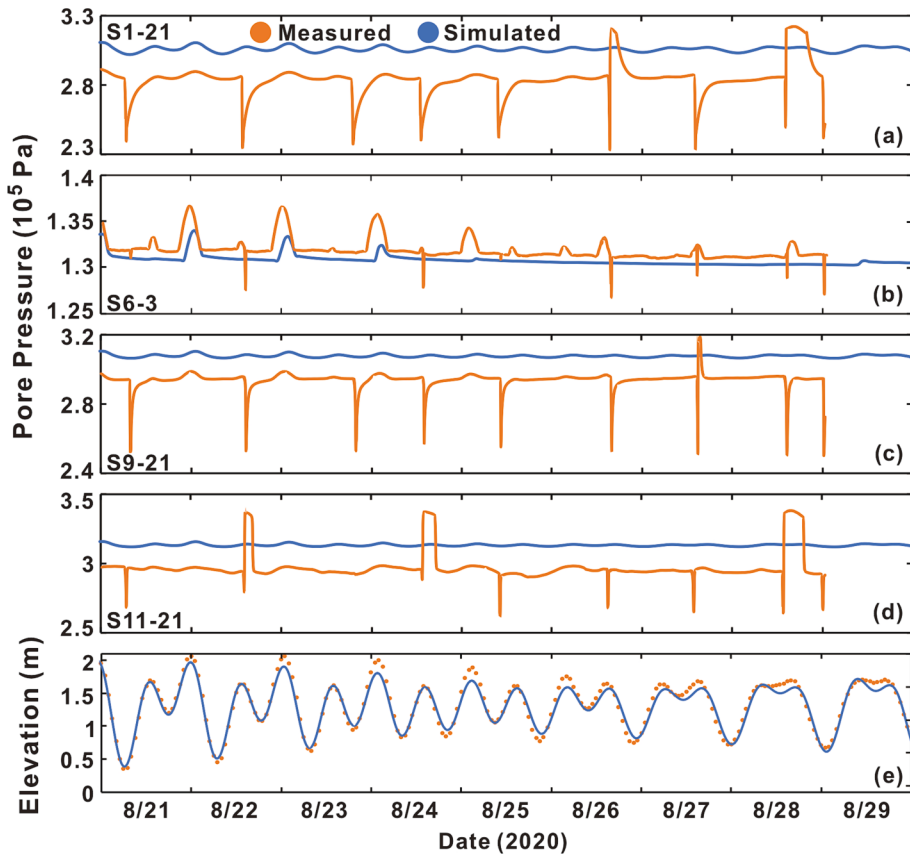


Fig. 7. Pore pressures and tide levels at the study site. a-d) Comparison of measured and modeled pore pressure at selected sampling locations, and e) Comparison of tidal station data (orange solid dots) with the predicted tidal signal (blue solid line) during the monitoring period. The elevation is relative to the local tidal datum. (For interpretation of the references to colour in this figure legend, the reader is referred to the web version of this article.)

dominant characteristic along the aquifer-ocean interface. Most mangrove trees at the site were located on the mangrove platform, and the seaward boundary of the platform was located at site S1 at an elevation of 1.3 m relative to the local tidal datum (equivalent to 0 m MSL). Hence, the intersection of MSL and the land surface defined the boundary between a *below MSL zone* and a *mangrove zone* (Fig. 8b). The landward boundary of the mangrove zone was where the platform elevation was 1.8 m. Farther inland, a third zone, "TC4" (Tidal Creek 4), spanned across the tidal creek that flows perpendicular to the sampling transect between wells S10 and S11. The locations of the three zones are depicted in Fig. 8b. Of the $0.40 \text{ m}^2/\text{d}$ of net outflow, 45% entered the *below MSL zone*, 33% discharged into the *mangrove zone*, and the remaining 22% discharged into TC4 zone (Table S1).

SGD into the tidal creeks along the sampling profile was computed to estimate the total volumetric discharge into tidal creeks in Dongzhai Harbor. The *below MSL zone* can be classified as a tidal creek, as Tidal Creek 3 bounds the west edge of the mangrove wetland. Thus, the SGD rate into the *below MSL zone* and TC4 zone, $0.14 \text{ m}^2/\text{d}$, can be taken as an

estimate of the SGD rate for tidal creeks surrounding the harbor. Extrapolating over the mangrove area (1750 ha) in Dongzhai Harbor and considering the density of tidal creeks within the same area (0.002 m/m^2 estimated from remote sensing images), we estimate a total discharge of $4.9 \times 10^3 \text{ m}^3/\text{d}$ into tidal creeks in the region. This compares with $1.2 \times 10^4 \text{ m}^3/\text{d}$ directly into mangrove forest platforms. Thus, discharge to mangrove platforms may be 2.5 times higher than to tidal creeks in Dongzhai Harbor.

The spatially averaged net outflow rate (m/d) into the tidal creeks along the sampling transect (i.e. the average rate in the *below MSL zone* and TC4 zone) and *mangrove zone* were compared to results of previous studies investigating fluid exchanges in mangroves. Table 3 shows that net outflow at our site was at the lower range measured in other studies. However, at our site there was significant spatial variability in net outflow/inflow rates across the ocean-aquifer interface and this variability was highest where there was high topographic relief (Fig. 8a). For instance from $76 \text{ m} < x < 84 \text{ m}$ net outflow reached $4 \times 10^{-3} \text{ m/d}$, which was about 6-fold higher than the spatially averaged rate of $6.7 \times$

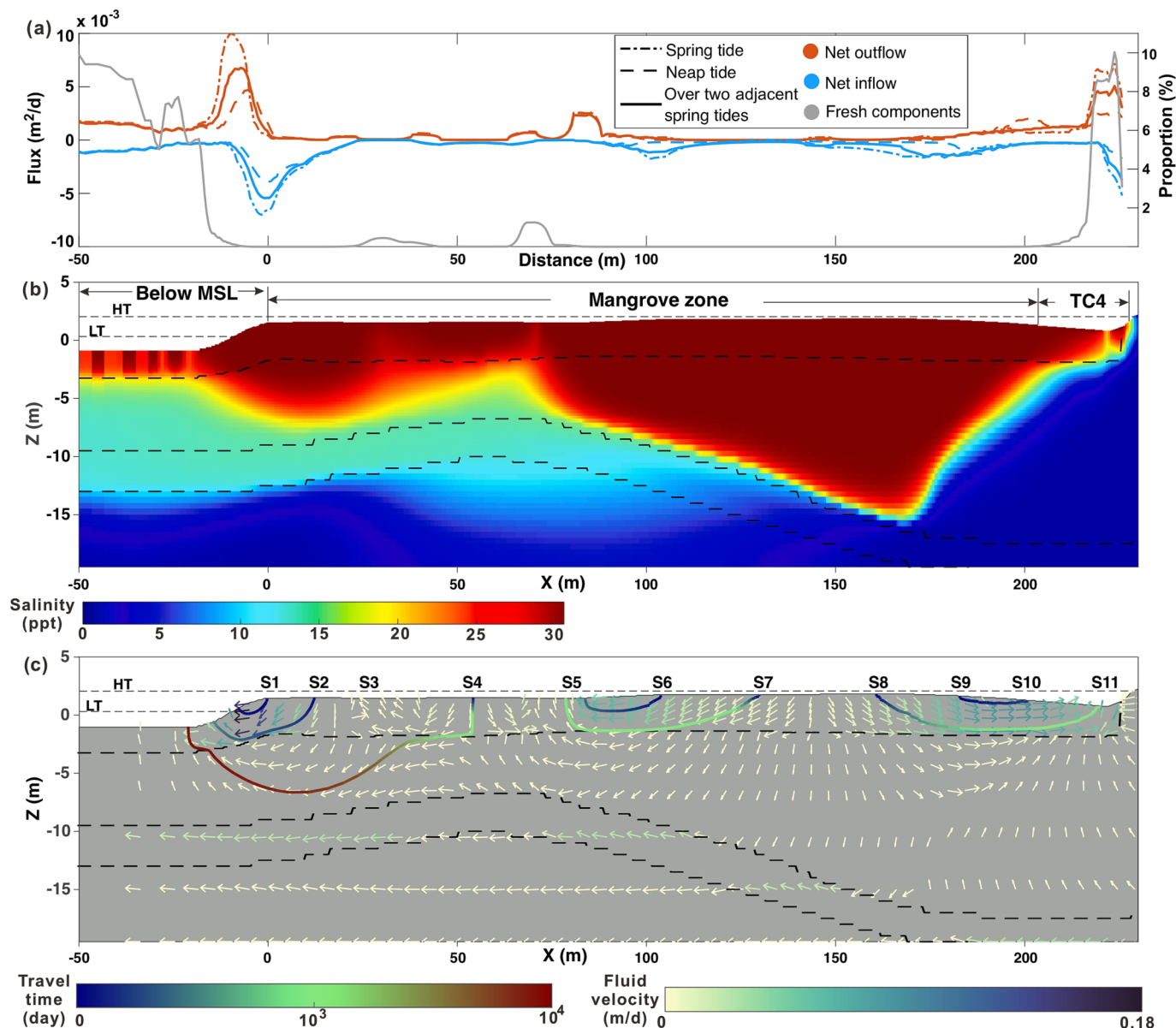


Fig. 8. Base model results. a) Net outflow and inflow and fresh SGD proportion along the aquifer-ocean interface. b) Salinity distribution. c) Flow vectors and streamlines originating from selected sampling sites. The black dashed lines in (b) and (c) are the interfaces between the geologic layers. The elevation is relative to the local tidal datum. Results show the flow field and salinity distribution averaged across a spring-neap cycle.

Table 3

Comparison of net outflow rates in this study to previous studies.

Study area	Spatially Averaged Net Outflow Rate (m/d)		Method	Reference
	Mangrove	Creek		
Clarence River estuary, Yamba	1.3×10^{-2}	3.4×10^{-2}	Radium isotope	Wadnerkar et al. (2021)
Daya Bay, China	6.2×10^{-4} – 1×10^{-3}	4×10^{-3} – 5×10^{-3}	Darcy's law	Xiao et al. (2018)
Dongzhai harbor, Hainan, China	6.7×10^{-4}	2.8×10^{-3}	Numerical model	This study
Zhangjiang Estuary, China	3.6×10^{-3} – 4.3×10^{-3}	n. a.	Darcy's law	Wang et al. (2022)
Australia	1.5×10^{-3} – 3×10^{-1}	n. a.	Radium isotope	Tait et al. (2017)
Tauranga and Waikareao Harbor, New Zealand	0.2	n. a.	Radon isotope	Santos et al. (2014)
Qinglan bay, Hainan, China	n. a.	1.65	Radon isotope	Wu et al. (2021)
Maowei Sea, China	n. a.	0.36	Radon isotope	Chen et al. (2018)
Southern Moreton Bay, Australia	n. a.	2.5×10^{-2}	Radon and radium isotope	Gleeson et al. (2013a,b)

Note: "n.a." indicates "not available". The rates reported in this study were calculated by dividing net outflow (m²/d) by the length (m) of the mangrove forest zone or creek.

10^{-4} m/d. The locally elevated discharge rates more closely approximated the mean rate (3.9×10^{-3} m/d) across all previous studies. These results indicate that high spatial variability of discharge rates should be considered when quantifying spatially averaged net outflow from mangroves. Estimates of average net outflow obtained from point measurements along more easily accessible mangrove edges (e.g. Wang et al. 2022) may over or under estimate outflow depending on local topographic relief and site conditions.

To further examine SGD patterns, we analyzed the freshwater discharge profile along the mangrove-aquifer interface. Freshwater discharge at each model cell was calculated by multiplying total discharge at the cell by the cell's fraction of freshwater. Over two adjacent spring tides, 42% of freshwater discharged to the *below MSL zone*, 57% of freshwater discharged to the *TC4 zone*, and only 1% of freshwater discharged to the *mangrove zone* (Fig. 8a; fresh components). Thus, discharge within the mangrove wetland was almost entirely tidally-driven saline groundwater circulation. Of the small volume of freshwater that discharged to the *mangrove zone*, much of it was focused near S3 and S5 at the edges of a mass of circulating saltwater (Fig. 8a-c). These areas were directly above the crest of the undulating high-permeability layer where freshwater continued an upward and seaward trajectory to the surface (Fig. 8c).

Half (51%) of seawater that infiltrated into the *mangrove zone* discharged out of the same zone; the remaining 49% discharged to tidal creeks. Seawater that infiltrated the *mangrove zone* circulated rapidly through the root zone (Layer 1) as shown by the tidally averaged streamlines in Fig. 8c. The residence time of circulating saltwater in the root zone (1,000 days) was significantly shorter than in the less permeable sediments of Layer 2 (10,000 days). However, a significant fraction (90%) of seawater that infiltrated the *mangrove zone* circulated only within Layer 1, with only 10% flowing into Layer 2. This indicates that most saline groundwater that discharged to the mangrove platform had a relatively short residence time and flowed only through the upper few meters of the aquifer.

The size of the saltwater-freshwater mixing area (subsurface where

salinity was between 10% and 90% seawater salinity) in the aquifer varied by less than 1 m² in response to tidal stage (12 h) and fortnightly spring-neap cycling in tidal amplitude (Fig. S6). The mixing zone was stable due in part due to the small amount of seawater that flowed from Layer 1 to Layer 2, where a large proportion of the mixing zone was located. The second factor that contributed to stable salinities was the low-permeability of Layer 2, which led to a negligible salinity change over the timescales of the overlying tidal forcing (Fig. S6).

4.3. Effects of topography and anisotropy on seawater-groundwater mixing

4.3.1. Topography

Mangrove topography was a major control affecting subsurface salinity distributions. Compared to the base case, model Case-T1 (uniform slope) and model Case-T2 (platform) resulted in substantially less salt mass in the subsurface (Fig. 9). Saline pore water in the case with a uniform slope extended to a depth of only 5 m below the surface (Fig. 9b). The results in the case with a platform were similar; however, a circular mass of saltwater formed below the area extending from the shoreface slope to a distance of 50 m inland (Fig. 9c). The flow vectors in Fig. 9c show that the inland extent of saltwater at x = 50 m was bounded by a zone of upward flowing fresh groundwater that was forced out of the high-permeability layer due to the bend in the layer's geometry.

Previous studies have explored the effects of multiple topographic profiles with uniform slopes on flow and transport in homogeneous sandy beach aquifers (Evans et al., 2020; Greskowiak, 2014). The studies revealed that topography has a controlling effect on subsurface salinity distributions. In this study, we demonstrate that the topographic profile in mangroves is similarly important for flow and mixing. Our results also capture the combined effects of topography and lithology. In both model cases with a constant slope and flat platform, the absence of local topographic relief produced a weak hydraulic gradient driving circulating saline flow. As a result, downward circulating salt was unable to penetrate into the lower permeability material in Layer 2 (Fig. 9b-c). The behavior of the low-permeability layer as a physical barrier to downward migration of salt is similar to the findings of Zhang et al. (2021b), in which simulations of salt transport in a beach aquifer showed that downward salt transport was restricted by the presence of a low-permeability layer.

Models with a uniform slope (Case-T1) and flat platform (Case-T2) both resulted in salt fingers in Layer 1 that extended to the bottom of the layer (Fig. 9b-c). Salt fingers formed in the upper 3 m of the aquifer in Case T1 (uniform slope) and upper 5 m in Case T2 (platform). Upward flow of freshwater between salt fingers produced in a pattern of fluctuating proportion of fresh SGD for both topographic profiles (Fig. 9a). Although fresh discharge between salt fingers produced a spatially variable fresh discharge pattern, total SGD was more spatially uniform than the base model because there was no local relief in either topographic scenario (Fig. 9a).

Previous studies have shown that vertical accretion rates can vary spatially within a single mangrove, with higher rates in areas where the density of mangrove trees is higher (Krauss et al., 2017; McIvor et al., 2013). The spatially heterogeneous vertical accretion rates can result in topographic relief across mangrove wetlands. Considering these previous findings as well as contrast in SGD patterns between the base case (Fig. 8b) and Case-T2 (Fig. 9b), our results suggest that higher topographic relief resulting from variable accretion would increase local hydraulic gradients and drive saltwater deeper into the mangrove subsurface.

4.3.2. Vertical anisotropy

The subsurface salinity distribution was generally insensitive to anisotropy of Layer 1, while groundwater discharge exhibited greater variability compared to the base model. An increase of anisotropy of Layer 1 from 1.0 to 0.1 (Case-P1), representing weaker development of

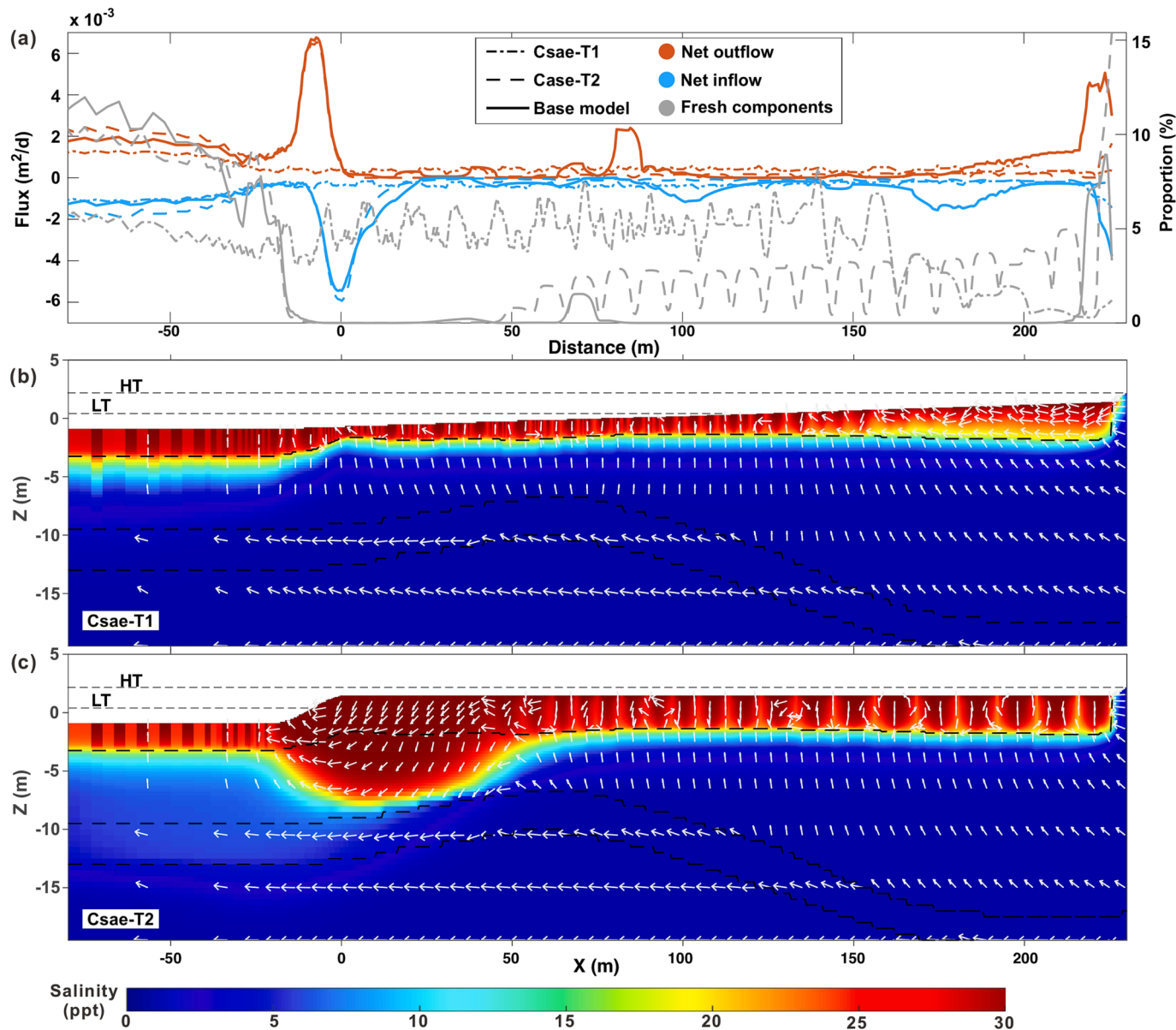


Fig. 9. Results of the Case-T models. a) Net outflow and inflow and fresh SGD proportion along the aquifer-ocean interface. b) Salinity distribution and flow velocity vectors in model Case-T1. c) Salinity distribution and flow velocity vectors in model Case-T2. The black dashed lines in (b) and (c) are the interfaces between the geologic layers. The elevation is relative to the local tidal datum. Results show the flow field and salinity distribution averaged across a spring-neap cycle.

vertical burrow channels in the surface layer, resulted in a slight overall decrease in salinity in shallow sediments under the bay and negligible change elsewhere (Fig. 10b). Conversely, the groundwater discharge pattern was muted and total discharge decreased by 40% ($0.054 \text{ m}^3/\text{d}$) relative to the base case due to the lower vertical permeability of Layer 1 (Fig. 10a).

In model Case-P2, where the anisotropy of Layer 2 was decreased from 0.05 to 0.1 to reflect more typical anisotropic conditions (i.e. no additional compaction from the 1605 earthquake), both groundwater salinity and discharge patterns deviated substantially from the base model (Fig. 10a and c). With only a slightly lower anisotropy (i.e. higher vertical permeability) in Layer 2, more saline groundwater entered the high-permeability layer, which prevented the preferential seaward flow of freshwater. This eliminated the hydraulic barrier effect of the high-permeability layer and allowed saltwater to flow to the base of the aquifer. Apart from a freshwater zone below the inland area of the mangrove ($x > 175 \text{ m}$), saltwater occupied the entirety of the aquifer system. As a result, all freshwater discharged near the high tide line at x

$= 220 \text{ m}$ (Fig. 10a). Interestingly, total inflow and outflow patterns were nearly identical to the base model across the mangrove platform despite the large differences in salinity distributions. The overlapping exchange profiles in Fig. 10a are a consequence of the shallow saltwater circulation patterns below the platform in both models. As discussed previously, most discharge to the mangrove in the base model was saltwater that circulated only through Layer 1, which was predominantly saline. In model Case-P2, the bulk of saltwater circulation was also confined to Layer 1, thus the spatial discharge patterns were similar. As a result, total discharge to surface water in Case-P2 was about the same (94% of base) as the base model ($3.81 \times 10^{-1} \text{ m}^3/\text{d}$ vs. $4.04 \times 10^{-1} \text{ m}^3/\text{d}$, respectively; Table S1 and S2). These results indicate that, based on our model setup, even a minor environmental change to anisotropy can have a strong impact on subsurface salinity distributions and fresh discharge patterns, but may not be a major control on total groundwater discharge from mangroves.

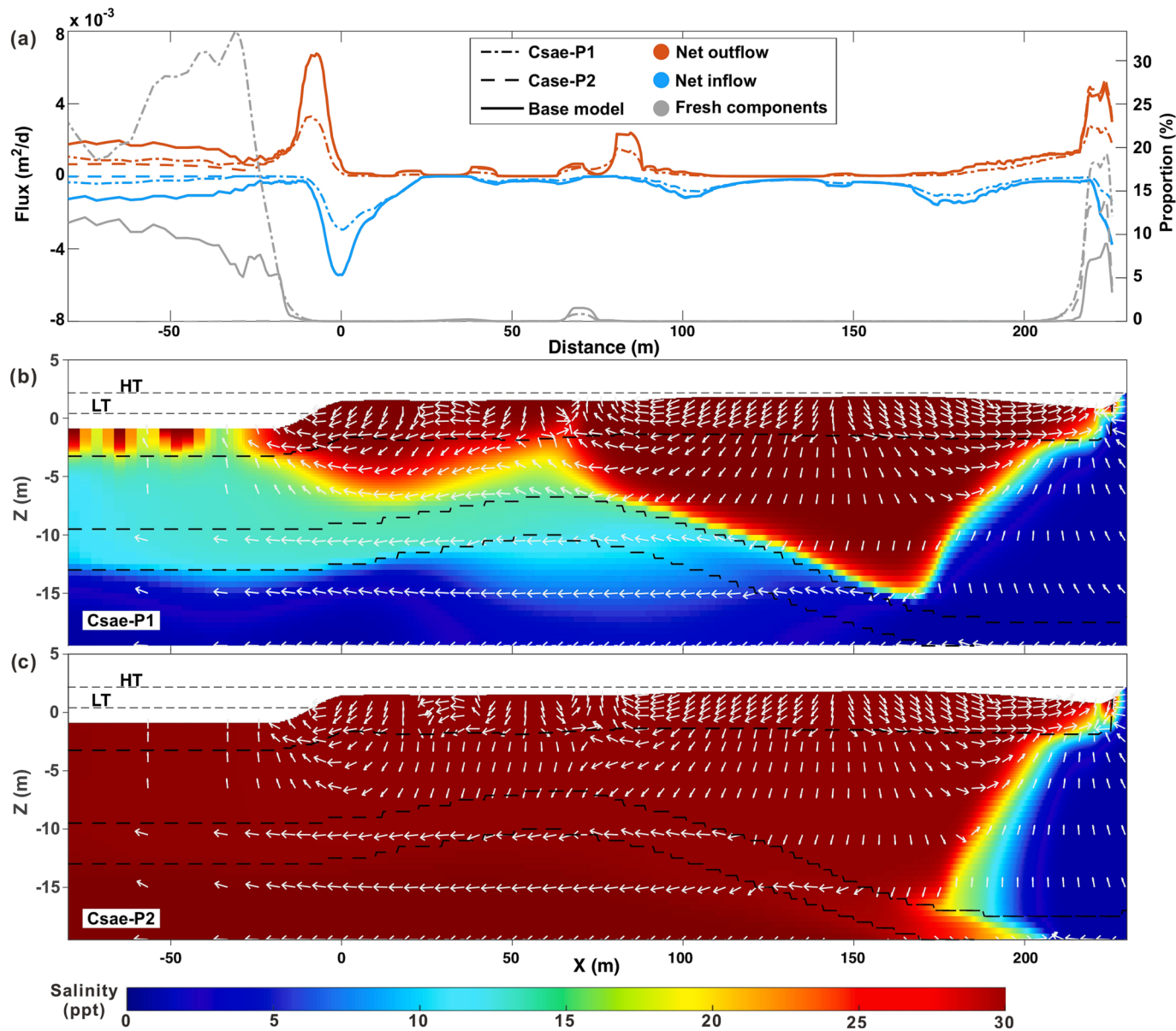


Fig. 10. Results of the Case-P models. a) Net outflow and inflow and fresh SGD proportion along the aquifer-ocean interface. Case-P2 outflow and inflow lines are not visible landward of $x = 25$ m due to overlap with the base case. b) Salinity distribution and flow velocity vectors in model Case-P1. c) Salinity distribution and flow velocity vectors in model Case-P2. The black dashed lines in (b) and (c) are the interfaces between the geologic layers. The elevation is relative to the local tidal datum. Results show the flow field and salinity distribution averaged across a spring-neap cycle.

4.4. Implications for understanding mangrove ecosystem responses

The salinity distributions and discharge patterns shown in this study can be used to provide insight into how mangroves may respond to storm events. Satellite images taken before and after typhoon *Rammasun* that passed through the study site in 2014 showed that mangrove growth near S3 and S5 has been gradually deteriorating since the storm (Fig. S5). The optimal growth conditions for seedlings of the dominant mangrove species at the site, *Rhizophora stylosa*, are where pore water is 5 ppt (Kodikara et al., 2017). The present study showed there are high pore water salinities (>20 ppt) in the area of the mangrove forest that was damaged by the typhoon. This suggests that mangrove recovery following the storm was inhibited by high pore water salinities that inhibited growth of mangrove seedlings. Moreover, the damaged mangrove area is in a zone of groundwater discharge (Fig. 8c) and groundwater discharging from mangroves can serve as a source of heavy metals (Li et al., 2022), which can negatively impact mangrove growth

and development (Sandilyan and Kathiresan, 2014; Yan et al., 2017). Thus, the accumulation of contaminants in the mangrove root zone may have led to mangroves trees that were of poor health and thus vulnerable to damage by storm activity. The results of this study may therefore provide a baseline for better understanding the role of subsurface hydrology and redox processes on affecting mangrove resilience to coastal storms and recovery following environmental perturbations.

4.5. Model limitations

The objective of this study was to investigate salinity distributions and fresh and saline groundwater discharge patterns in a mangrove aquifer system. While the measured and modeled salinities matched well over the measurement period, there are factors that can affect aquifer salinity and groundwater discharge over periods that were not considered in this study. Additionally, we did not measure groundwater discharge at the site, thus the modeled discharges and salinity

distributions are based on a number of simplifying model assumptions.

The models did not consider seasonal variations to freshwater hydraulic head (Fang et al., 2022; Liu et al., 2016) or the effects of pumping on water levels (Xiao et al., 2021). In highly permeable beach aquifers, these transient hydrologic forcings can lead to dynamic intertidal saltwater-freshwater mixing zones and time-varying discharge rates across sediment–water interfaces. However, such responses are likely less pronounced in low-permeability mangroves compared to sandy beaches, as was the case at our field site. This study also neglected evapotranspiration and salt rejection by mangroves (McGowan and Martin, 2007), which increases the salinity of pore water surrounding mangrove roots as shown in this study, potentially affecting density-driven flow patterns. In addition, benthic burrows were not explicitly resolved (Xin et al., 2009) and preferential flow through such burrows can affect tidally driven seawater circulation (Xiao et al., 2019b). Although these mechanisms and features were not represented in our models, the simulations reproduced the measured salinities and pore pressures, indicating that the model sufficiently captured the key hydrological processes and geologic structure controlling flow and salt transport in the mangrove subsurface.

5. Conclusion

This study combined numerical variable-density variably-saturated groundwater flow and salt transport models with high resolution pore water sampling to examine salinity distributions and submarine groundwater discharge patterns in a mangrove aquifer influenced by tides. A cross-shore multi-level groundwater monitoring profile was used to measure salinity and pore pressure through three sampling periods over one year. Salinity and pore pressure measurements and lithologic data were used to calibrate models for exploring the influence of mangrove topography and anisotropy on saltwater-freshwater mixing and fresh and saline groundwater discharge patterns in the mangrove wetland.

Both the measurements and models showed that a saltwater-freshwater mixing zone formed below the mangrove platform due to seawater infiltration and mixing with underlying fresh groundwater. The bottom of the mixing zone was bounded by a high-permeability sand layer that channeled freshwater offshore and served as a hydraulic barrier to downward salt transport. The sediment–water interface below mean sea level received the highest proportion (45%) of total groundwater discharge, followed by the mangrove platform (33%) and a nearby tidal creek (22%). Only 1% of fresh groundwater discharged to the mangrove platform, indicating that discharge to the mangrove ecosystem was nearly all tidally driven saline circulation. Moreover, 90% of saline discharge to the mangrove platform circulated only within the shallow mangrove root layer, with only 10% entering deeper strata.

Model sensitivity tests showed that saltwater-freshwater mixing and groundwater discharge patterns were sensitive to mangrove topography and aquifer anisotropy. Topographic surfaces with little to no relief resulted in muted discharge profiles and substantially less salt mass in the aquifer due to weaker local topographically-driven hydraulic gradients. Analysis of controls of aquifer anisotropy demonstrated the potentially important role of a recent earthquake on sediment compaction and subsurface salinity patterns at the field site. These insights of the spatial variability of aquifer salinity and fresh and saline groundwater discharge patterns may aid in preserving and managing mangroves and other coastal ecosystems threatened by sea level rise and coastal population growth.

CRediT authorship contribution statement

Kang Peng: Conceptualization, Investigation, Methodology, Formal analysis, Writing – original draft, Writing – review & editing. **James W. Heiss:** Writing – original draft, Supervision, Writing – review & editing. **Xianjun Xie:** Conceptualization, Supervision, Funding acquisition. **Lu**

Yan: Investigation, Methodology. **Yamin Deng:** Project administration, Funding acquisition. **Yiqun Gan:** Project administration. **Qinghua Li:** Funding acquisition. **Yanpeng Zhang:** Resources.

Declaration of Competing Interest

The authors declare that they have no known competing financial interests or personal relationships that could have appeared to influence the work reported in this paper.

Data availability

Data will be made available on request.

Acknowledgments

The research work was financially supported by National Natural Science Foundation of China (42020104005; U2244225), National Key Research and Development Program of China (2021YFA0715900), the Ministry of Education of China (111 project), and the Fundamental Research Funds for the Central Universities, China University of Geosciences (Wuhan) and China Geological Survey (DD20211391). The authors acknowledge the MIT SuperCloud and Lincoln Laboratory Supercomputing Center for providing HPC resources and assistance for running model simulations.

Appendix A. Supplementary data

Supplementary data to this article can be found online at <https://doi.org/10.1016/j.jhydrol.2023.129472>.

References

- Alongi, D.M., Brinkman, R., 2011. Hydrology and Biogeochemistry of Mangrove Forests, Forest Hydrology and Biogeochemistry. Springer, pp. 203–219.
- Alongi, D.M., Sasekumar, A., 1992. Benthic communities. Geophysical Union.
- Burnett, W.C., Aggarwal, P.K., Aureli, A., Bokuniewicz, H., Cable, J.E., Charette, M.A., Kontar, E., Krupa, S., Kulkarni, K.M., Loveless, A., Moore, W.S., Oberdorfer, J.A., Oliveira, J., Ozyurt, N., Povinec, P., Privitera, A.M.G., Rajar, R., Ramessur, R.T., Scholten, J., Stiegitz, T., Taniguchi, M., Turner, J.V., 2006. Quantifying submarine groundwater discharge in the coastal zone via multiple methods. *Sci. Total Environ.* 367 (2–3), 498–543.
- Chang, S., Wang, X., 2002. Courant number insensitive CE/SE Euler scheme. In: 38th AIAA/ASME/SAE/ASEE Joint Propulsion Conference & Exhibit (p. 3890).
- Chen, N., 2020. Mapping mangrove in Dongzhaiyang, China using Sentinel-2 imagery. *J. Appl. Remote Sens.* 14 (1), 11.
- Chen, X., Zhang, F., Lao, Y., Wang, X., Du, J., Santos, I.R., 2018. Submarine groundwater discharge-derived carbon fluxes in mangroves: an important component of blue carbon budgets? *J. Geophys. Res. Oceans* 123 (9), 6962–6979.
- Evans, T.B., White, S.M., Wilson, A.M., 2020. Coastal groundwater flow at the nearshore and embayment scales: A field and modeling study. *Water Resour. Res.* 56 (10).
- Fang, Y., Zheng, T., Wang, H., Zheng, X., Walther, M., 2022. Influence of dynamically stable-unstable flow on seawater intrusion and submarine groundwater discharge over tidal and seasonal cycles. *J. Geophys. Res. Oceans* 127 (4).
- Ferris, J.G., 1952. Cyclic Fluctuations of Water Level as a Basis for Determining Aquifer Transmissibility. US Dept of the Interior Geological Survey Water Resources Division.
- Gelhar, L.W., Welty, C., Rehfeldt, K.R., 1992. A critical review of data on field-scale dispersion in aquifers [J]. *Water resources research* 28 (7), 1955–1974.
- Geng, X., Heiss, J.W., Michael, H.A., Boufadel, M.C., Lee, K., 2020. Groundwater flow and moisture dynamics in the Swash Zone: Effects of heterogeneous hydraulic conductivity and capillarity. *Water Resour. Res.* 56 (11).
- Gleeson, J., Santos, I.R., Maher, D.T., Golsby-Smith, L., 2013a. Groundwater-surface water exchange in a mangrove tidal creek: Evidence from natural geochemical tracers and implications for nutrient budgets. *Mar. Chem.* 156, 27–37.
- Gleeson, J., Santos, I.R., Maher, D.T., Golsby-Smith, L., 2013b. Groundwater-surface water exchange in a mangrove tidal creek: Evidence from natural geochemical tracers and implications for nutrient budgets. *Mar. Chem.* 156, 27–37.
- Greskowiak, J., 2014. Tide-induced salt-fingering flow during submarine groundwater discharge. *Geophys. Res. Lett.* 41 (18), 6413–6419.
- Hammond, G.E., Lichtner, P.C., Mills, R., 2014. Evaluating the performance of parallel subsurface simulators: An illustrative example with PFLOTRAN. *Water Resour. Res.* 50 (1), 208–228.
- Heiss, J.W., 2014. Saltwater-Freshwater Mixing Dynamics in a Sandy Beach Aquifer Over Tidal, Spring-Neap, And Seasonal Cycles.

- Hou, Y., Yang, J., Russoiello, C.J., Zheng, T., Wu, M.L., Yu, X., 2022. Impacts of coastal shrimp ponds on saltwater intrusion and submarine groundwater discharge. *Water Resources Research* 58 (7), e2021WR031866.
- Kodikara, K.A.S., Jayatissa, L.P., Huxham, M., Dahdouh-Guebas, F., Koedam, N., 2017. The effects of salinity on growth and survival of mangrove seedlings changes with age. *Acta Bot. Bras.* 32 (1), 37–46.
- Krauss, K.W., Cormier, N., Osland, M.J., Kirwan, M.L., Stagg, C.L., Nestlerode, J.A., Russell, M.J., From, A.S., Spivak, A.C., Dantin, D.D., Harvey, J.E., Almario, A.E., 2017. Created mangrove wetlands store belowground carbon and surface elevation change enables them to adjust to sea-level rise. *Sci. Rep.* 7 (1), 1030.
- Levanon, E., Yechieli, Y., Gvirtzman, H., Shalev, E., 2017. Tide-induced fluctuations of salinity and groundwater level in unconfined aquifers – Field measurements and numerical model. *J. Hydrol.* 551, 665–675.
- Li, Z., Pan, F., Xiao, K., Li, H., Zheng, C., Wang, X., Zhang, Y., Wang, Q., Zhang, L., 2022. An integrated study of the spatiotemporal character, pollution assessment, and migration mechanism of heavy metals in the groundwater of a subtropical mangrove wetland. *J. Hydrol.* 612.
- Liu, Y., Jiao, J.J., Luo, X., 2016. Effects of inland water level oscillation on groundwater dynamics and land-sourced solute transport in a coastal aquifer. *Coast. Eng.* 114, 347–360.
- Manga, M., Wang, C.Y., 2015. 4.12 - Earthquake Hydrology [M]//Schubert, G. Treatise on Geophysics, Second Edition. Elsevier, Oxford, pp. 305–328.
- Marois, D.E., Stecher, H.A., 2020. A simple, dynamic, hydrological model for mesotidal salt marshes. *Estuar. Coast. Shelf Sci.* 233, 106486.
- McGowan, K.T., Martin, J.B., 2007. Chemical composition of mangrove-generated brines in Bishop Harbor, Florida: Interactions with submarine groundwater discharge. *Mar. Chem.* 104 (1–2), 58–68.
- McIvor, A.L., Spencer, T., Möller, I., Spalding, M., 2013. The response of mangrove soil surface elevation to sea level rise. *Nature Conserv. Wetlands Int.*
- Moffett, K.B., Gorelick, S.M., McLaren, R.G., Sudicky, E.A., 2012. Salt marsh ecohydrological zonation due to heterogeneous vegetation–groundwater–surface water interactions. *Water Resour. Res.* 48 (2).
- Moore, W.S., 2010. The effect of submarine groundwater discharge on the ocean. *Ann. Rev. Mar. Sci.* 2 (1), 59–88.
- Reeves, H.W., Thibodeau, P.M., Underwood, R.G., Gardner, L.R., 2000. Incorporation of total stress changes into the ground water model SUTRA. *Ground Water* 38 (1), 89–98.
- Reuther, A., Kepner, J., Byun, C., Samsi, S., Arcand, W., Michaleas, P., 2018. Interactive supercomputing on 40,000 cores for machine learning and data analysis. *IEEE*.
- Robinson, C., Xin, P., Li, L., Barry, D.A., 2014. Groundwater flow and salt transport in a subterranean estuary driven by intensified wave conditions [J]. *WATER RESOURCES RESEARCH* 50 (1), 165–181.
- Robinson, C.E., Xin, P., Santos, I.R., Charette, M.A., Li, L., Barry, D.A., 2018. Groundwater dynamics in subterranean estuaries of coastal unconfined aquifers: Controls on submarine groundwater discharge and chemical inputs to the ocean. *Adv. Water Resour.* 115, 315–331.
- Sandilyan, S., Kathiresan, K., 2014. Decline of mangroves – A threat of heavy metal poisoning in Asia. *Ocean Coast. Manag.* 102, 161–168.
- Santos, I.R., Burnett, W.C., Dittmar, T., Suryaputra, I., Chanton, J., 2009. Tidal pumping drives nutrient and dissolved organic matter dynamics in a Gulf of Mexico subterranean estuary. *Geochim. Cosmochim. Acta* 73 (5), 1325–1339.
- Santos, I.R., Bryan, K.R., Pilditch, C.A., Tait, D.R., 2014. Influence of porewater exchange on nutrient dynamics in two New Zealand estuarine intertidal flats. *Mar. Chem.* 167, 57–70.
- Santos, I.R., Chen, X., Lecher, A.L., Sawyer, A.H., Moosdorf, N., Rodellas, V., Tamborski, J., Cho, H.-M., Dimova, N., Sugimoto, R., Bonaglia, S., Li, H., Hajati, M.-C., Li, L., 2021. Submarine groundwater discharge impacts on coastal nutrient biogeochemistry. *Nature Rev. Earth Environ.* 2 (5), 307–323.
- Schwartz, R.C., Evett, S.R., Unger, P.W., 2003. Soil hydraulic properties of cropland compared with reestablished and native grassland. *Geoderma* 116 (1–2), 47–60.
- Shen, C., Zhang, C., Jin, G., Kong, J., Li, L., 2016. Effects of unstable flow on solute transport in the marsh soil and exchange with coastal water. *Geophys. Res. Lett.* 43 (23).
- Shen, C., Zhang, C., Kong, J., Xin, P., Lu, C., Zhao, Z., Li, L., 2019. Solute transport influenced by unstable flow in beach aquifers. *Adv. Water Resour.* 125, 68–81.
- Shi, L., Jiao, J.J., 2014. Seawater intrusion and coastal aquifer management in China: a review. *Environ. Earth Sci.* 72 (8), 2811–2819.
- Tait, D.R., Maher, D.T., Sanders, C.J., Santos, I.R., 2017. Radium-derived porewater exchange and dissolved N and P fluxes in mangroves. *Geochim. Cosmochim. Acta* 200, 295–309.
- Todd, D.K., Mays, L.W., 2004. Groundwater Hydrology, 3rd edition.
- Tully, K., Gedan, K., Epanchin-Niell, R., Strong, A., Bernhardt, E.S., BenDor, T., Mitchell, M., Kominoski, J., Jordan, T.E., Neubauer, S.C., Weston, N.B., 2019. The invisible flood: The chemistry, ecology, and social implications of coastal saltwater intrusion. *Bioscience* 69 (5), 368–378.
- Voss, C.I., Provost, A., 2002. SUTRA: A model for 2D or 3D saturated-unsaturated, variable-density ground-water flow with solute or energy transport. *Water-Resour. Invest. Report* 2002-4231.
- Wadnerkar, P.D., Batsaikhan, B., Conrad, S.R., Davis, K., Correa, R.E., Holloway, C., White, S.A., Sanders, C.J., Santos, I.R., 2021. Contrasting radium-derived groundwater exchange and nutrient lateral fluxes in a natural mangrove versus an artificial canal. *Estuar. Coasts* 44 (1), 123–136.
- Wang, F., Xiao, K., Santos, I.R., Lu, Z., Tamborski, J., Wang, Y., Yan, R., Chen, N., 2022. Porewater exchange drives nutrient cycling and export in a mangrove-salt marsh ecotone. *J. Hydrol.* 606.
- Weinstein, Y., Yechieli, Y., Shalem, Y., Burnett, W.C., Swarzenski, P.W., Herut, B., 2011. What is the role of fresh groundwater and recirculated seawater in conveying nutrients to the coastal ocean? *Environ. Sci. Technol.* 45 (12), 5195–5200.
- Wilson, A.M., Gardner, L.R., 2006. Tidally driven groundwater flow and solute exchange in a marsh: Numerical simulations. *Water Resour. Res.* 42 (1).
- Wilson, A.M., Morris, J.T., 2012. The influence of tidal forcing on groundwater flow and nutrient exchange in a salt marsh-dominated estuary. *Biogeochemistry* 108 (1–3), 27–38.
- Wu, Z., Zhu, H., Tang, D., Wang, Y., Zidan, A., Cui, Z., 2021. Submarine groundwater discharge as a significant export of dissolved inorganic carbon from a mangrove tidal creek to Qinglan Bay (Hainan Island, China). *Cont. Shelf Res.*, 223.
- Xia, Y.Q., Li, H.L., 2012. A combined field and modeling study of groundwater flow in a tidal marsh. *Hydro. Earth Syst. Sci.* 16 (3), 741–759.
- Xiao, K., Li, H., Shananan, M., Zhang, X., Wang, X., Zhang, Y., Zhang, X., Liu, H., 2019a. Coastal water quality assessment and groundwater transport in a subtropical mangrove swamp in Daya Bay, China. *Sci. Total Environ.* 646, 1419–1432.
- Xiao, H., Tang, Y., Li, H., Zhang, L., Ngo-Duc, T., Chen, D., Tang, Q., 2021. Saltwater intrusion into groundwater systems in the Mekong Delta and links to global change. *Adv. Clim. Chang. Res.* 12 (3), 342–352.
- Xiao, K., Wu, J., Li, H., Hong, Y., Wilson, A.M., Jiao, J.J., Shananan, M., 2018. Nitrogen fate in a subtropical mangrove swamp: Potential association with seawater-groundwater exchange. *Sci. Total Environ.* 635, 586–597.
- Xiao, K., Wilson, A.M., Li, H., Ryan, C., 2019b. Crab burrows as preferential flow conduits for groundwater flow and transport in salt marshes: A modeling study. *Adv. Water Resour.* 132.
- Xin, P., Jin, G., Li, L., Barry, D.A., 2009. Effects of crab burrows on pore water flows in salt marshes. *Adv. Water Resour.* 32 (3), 439–449.
- Xin, P., Kong, J., Li, L., Barry, D.A., 2012. Effects of soil stratigraphy on pore-water flow in a creek-marsh system. *J. Hydrol.* 475, 175–187.
- Xin, P., Wilson, A., Shen, C., Ge, Z., Moffett, K.B., Santos, I.R., Chen, X., Xu, X., Yau, Y.Y., Moore, W., Li, L., 2022. Surface water and groundwater interactions in salt marshes and their impact on plant ecology and coastal biogeochemistry. *Rev. Geophys.* 60 (1) e2021RG000740.
- Yan, L., Guizhu, C., 2007. Physiological adaptability of three mangrove species to salt stress. *Acta Ecol. Sin.* 27 (6), 2208–2214.
- Yan, Z., Sun, X., Xu, Y., Zhang, Q., Li, X., 2017. Accumulation and tolerance of mangroves to heavy metals: a review. *Curr. Pollut. Reports* 3 (4), 302–317.
- Yan, L., Xie, X., Peng, K., Wang, N., Zhang, Y., Deng, Y., Gan, Y., Li, Q., Zhang, Y., 2021. Sources and compositional characterization of chromophoric dissolved organic matter in a Hainan tropical mangrove-estuary. *J. Hydrol.* 600.
- Zhang, M., Hao, Y., Zhao, Z., Wang, T., Yang, L., 2020. Estimation of coastal aquifer properties: A review of the tidal method based on theoretical solutions [J]. *WIREs Water* 8 (1).
- Zhang, M., Hao, Y., Zhao, Z., Wang, T., Yang, L., 2021a. Estimation of coastal aquifer properties: A review of the tidal method based on theoretical solutions. *Wiley Interdiscip. Rev. Water* 8 (1), e1498.
- Zhang, J., Lu, C., Shen, C., Zhang, C., Kong, J., Li, L., 2021b. Effects of a low-permeability layer on unstable flow pattern and land-sourced solute transport in coastal aquifers. *J. Hydrol.* 598.

Further reading

- Robinson, C., Gibbes, B., Carey, H., Li, L., 2007a. Salt-freshwater dynamics in a subterranean estuary over a spring-neap tidal cycle. 112(C9).
- Robinson, C., Li, L., Barry, D.A., 2007b. Effect of tidal forcing on a subterranean estuary. *Adv. Water Resour.* 30 (4), 851–865.
- Stieglitz, T., 2005. Submarine groundwater discharge into the near-shore zone of the Great Barrier Reef. Australia. *Mar Pollut Bull* 51 (1–4), 51–59.